Flash sintering of stoichiometric and hyper-stoichiometric urania

J.A. Valdez [a, *], D.D. Byler [a], E. Kardoulaki [a], J.S.C. Francis [b], K.J. McClellan [a]

[a] Los Alamos National Laboratory, Los Alamos, NM, 87545, USA
[b] Lupine Laboratories, Boulder, CO, 80301, USA

ABSTRACT

Flash sintering (FS), a novel fabrication technique belonging to the family of field assisted sintering (FAS) techniques, has been utilized in this study to fabricate uranium dioxide (UO_2) pellets. Stoichiometric ($UO_{2.00}$) and hyper-stoichiometric ($UO_{2.16}$) pellets were flash sintered at 600 °C within a few (2–3) minutes. This is in sharp contrast to conventional sintering where temperatures hundreds of degrees higher are necessary and the sintering time extends to hours. Relating this in terms of the homologous temperature ratio (T_H) for both conditions shows that in the case of flash sintering at 600 °C, $T_H = 0.3$ versus $T_H = 0.6$ for conventional sintering at 1600 °C. The highest density achieved for a $UO_{2.00}$ pellet was 81% theoretical density (TD) when flash sintered at 600 °C for 185 s at a field of 188 V/cm and a current density of 442 mA/mm^2. For the $UO_{2.16}$ pellet, the highest achieved density was 91% TD when flash sintered at 600 °C for 123 s at a field of 188 V/cm and a current density of 632 mA/mm^2. X-ray diffraction (XRD) characterization of the sintered pellets showed the final sintered material to be single cubic fluorite phase. Scanning electron microscopy (SEM) of longitudinal sections revealed non-uniform microstructures with regions of high density where the grain size ranged from 1 to 15 μm. Comparisons between conventionally and flash sintered pellets that achieved equivalent shrinkage strains were also conducted. In all cases, the flash sintered pellets achieved similar densification to the conventionally sintered pellets at much lower furnace temperatures and shorter times.

Published by Elsevier B.V.

1. Introduction

Field assisted sintering (FAS) techniques describe a group of novel sintering methods that use electric field and/or current to provide powder densification in very short time periods (minutes compared to hours) and at lower temperatures compared to conventional sintering [1]. Spark plasma sintering (SPS) [2–6] and flash sintering (FS) [7–20] are FAS methods that have received a lot of attention in recent years due to their potential significant economic impact. SPS uses a combination of temperature, pressure, and electric current to sinter powder compacts at lower temperatures and at shorter times but with better mechanical properties. In SPS, powder is loaded into a graphite die and heated by a pulsed direct current (DC) while simultaneously applying uniaxial pressure. Typically, the applied field is low (~volts) and the current flow through the die is high (~thousands of amps) [2]. FS, while similar to SPS (they both utilize field and current to induce densification), uses applied fields (1–100's of volts) and low current flow through the sample (amps). In FS, a low density powder compact sample is placed in a furnace, in contact with two electrical leads that are attached to a power supply, examples of this are shown in Refs. [7–19]. The flash event is characterized by a current runaway, during which the current exponentially increases before reaching a pre-defined current limit. The bulk of sintering can occur on the order of seconds under the application of appropriate fields, current densities and temperatures [21]. This is in contrast to conventional methods where any advances in lowering the sintering temperature to improve efficiency [22–24] still require long sintering times (hours) since the process is diffusion controlled.

FS has been demonstrated for a plethora of oxide materials such as ZrO_2 [9], an ionic conductor, $SrTiO_3$ [15], an insulator, TiO_2 [25], a semiconductor, and Y_2O_3 [26] and MgO-doped alumina [27], both wide band-gap insulators. However, little research has been conducted on its use as a fabrication method for nuclear fuels and specifically, UO_2. A recent study by Raftery et al. [28] has showcased that UO_2 can be flashed and that the onset conditions for flash sintering are dependent upon the applied field and furnace

---

* Corresponding author. Los Alamos National Laboratory, Materials Science and Technology Division, Mail-Stop G755, Los Alamos, NM, 87545, USA.
E-mail address: javaldez@lanl.gov (J.A. Valdez).

temperature. In fact, flash of $UO_{2.00}$ and UO_{2+x} was observed for a range of temperatures with the lowest being room temperature, unlike other ceramics [29]. This is not surprising as UO_2 is a semiconductor with a band gap of ~2eV [30] and its conductivity increases with temperature, therefore enabling a thermal runaway phenomenon that leads to the flash event. The similarities between UO_2 and ZrO_2, both are fluorite with a high melting point and can accommodate substantial oxygen non-stoichiometry depending on temperature and oxygen partial pressure as shown in the UO_2 phase diagram adapted from Ref. [31] in Fig. 1, (which highlights the $UO_{2+x}-U_4O_{9-y}$ phase field) indicated that flash sintering would be a fabrication technique applicable to UO_2. Additionally, the higher band gap of ZrO_2, ~6eV [32,33], versus ~2eV for UO_2, indicated that flash sintering in UO_2 could be applied at lower temperatures and fields to produce dense pellets.

In this work, flash sintering at a furnace temperature of 600 °C (a temperature where conventional sintering does not take place) was used to fabricate stoichiometric $UO_{2.00}$ and hyper-stoichiometric $UO_{2.16}$ pellets. Firstly, the conditions (applied field and current density) that produce the highest density pellets were identified. Subsequently, the sintered materials were characterized via X-ray diffraction (XRD) and scanning electron microscopy (SEM). Finally, comparisons between conventionally and flash sintered pellets that reached similar densification were conducted and showcase the potential of flash sintering as a fabrication method for UO_2 fuel as significantly lower temperatures and times are required.

2. Materials and methods

2.1. Materials preparation

Depleted uranium dioxide feedstock from AREVA with an oxygen to metal (O/M) ratio of 2.16 was used for this study. Stoichiometric uranium dioxide powder was also prepared by heat treating the as-received powder in flowing an argon-6% hydrogen gas mixture at 850 °C for 6 h, a methodology similar to ASTM C1430-07 [34]. The resulting material was evaluated to possess a nominal stoichiometry of $UO_{2.00}$. Both the $UO_{2.16}$ and $UO_{2.00}$ feedstocks were milled for 15 min in a Spex Certiprep 8100 high-energy mill with a zirconia ball and vial set and then sieved through a 325-mesh sieve.

Therefore the agglomerate size was nominally <44 μm but the particle size for both feedstocks was sub-micron.

X-ray diffraction (XRD) measurements were done on the as-received ($UO_{2.16}$) and the fully reduced ($UO_{2.00}$) powders to determine the phase of the starting materials using a Bruker AXS D8 Advance X-ray diffractometer. Peak indexing of the XRD pattern was performed using Bruker AXS's Evaluation (EVA) program [35] combined with the Joint Committee for Powder Diffraction Studies database [36].

The $UO_{2.16}$ and $UO_{2.00}$ feedstocks were cold pressed to produce $UO_{2.16}$ and $UO_{2.00}$ pellets, 4.49 mm in diameter and approximately 6 mm mm in height. Cylindrical pellets were used in this study as, unlike the dogbone samples frequently used in the literature [8,9,12,15,19,26,27,37,38], pellet geometry is the typical form for UO_2 fuel. It is also worth noting that no binder was used in cold pressing the pellets to avoid introducing any variables that could mask the material response during FS. This resulted in extremely delicate pellets that required absolute care during handling, especially in the case of the $UO_{2.00}$ pellets. For this reason, the $UO_{2.00}$ pellets were pressed at 60 MPa to achieve sufficient mechanical integrity, resulting in green densities of 7.09 g/cm³ (65% TD), while the $UO_{2.16}$ pellets only required pressing at 40 MPa, resulting in green densities of 5.94 g/cm³ (58% TD). The volume of the as pressed pellets used for geometric density determination was calculated based on an ideal cylindrical geometry. Finally, the ends of each pellet were coated with a thin film of platinum paint for a consistent interface with the electrical contacts.

2.2. Flash sintering set up and methods

In its simplest form, the apparatus used to perform the FS experiments consists of a furnace connected to a power supply via leads in contact with a sample. In this work, a Netzsch dilatometer (model DIL 402C) was adapted by retrofitting platinum leads and contacts, connected to a power supply (TDK LAMBDA model GEN300-11-1P230), to apply an electric field through the sample, which is in contact with the leads. This FS set up is similar to the one used by Hao et al. [39]. Adapting the dilatometer to perform FS was a natural fit since the dilatometry technique measures changes in length of a material as it is heated. A schematic and a photo
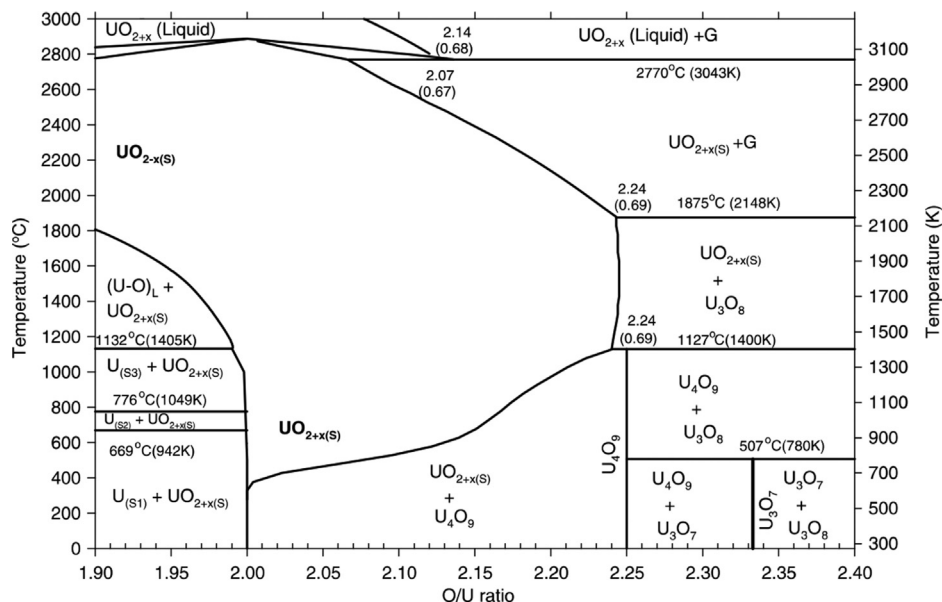

Fig. 1. Calculated U-O phase diagram, adapted from Higgs et al. [31] highlighting the $UO_{2+x}-U_4O_{9-y}$ phase field.

illustrating the experimental set up are shown in Fig. 2(a) and (b). The dilatometer was connected to a Centorr Model 2A gas purifier with an oxygen monitor to condition the flowing argon atmosphere during measurements to an oxygen content of 1×10^{-15} ppm. The pellets were heated in the dilatometer at a rate of 10 °C/min to an isothermal temperature of 600 °C and were held for 10 min to equilibrate the sample at temperature before application of the electric field.

In these experiments, when the electric field is applied to the specimens at 600 °C the power supply operates under voltage control. Upon application of the electric field across the pellet, the sintering process is initiated, which is accompanied by a nonlinear increase in the electrical conductivity (drop in resistance, R) of the specimen such that the current in the specimen rises instantaneously. This rapid rise in current triggers the power supply to drop in voltage due to the change in the specimen's resistance and switch into current control mode saturating at a maximum pre-set current limit. The power generation in the specimen equals to V^2/R during the voltage, V, controlled mode, meaning that the drop in resistance, R, leads to increased power generation, and therefore heating. When the mode switches to current control, and the current through the sample is steady at the maximum pre-defined value, the power generation is $I^2 \cdot R$ (I is the current) meaning that the heating is controlled by the applied current. The details of the process in which application of electric field/current leads to ultrafast sintering in zirconia are discussed in the work by Francis et al. [40].

Various fields and current densities were applied before the conditions that resulted in the highest density pellets, different for each stoichiometry, were identified. As such, only these conditions will be discussed in the following section. One must note other samples sintered under higher current densities than the ones discussed here may have produced higher local densities but these samples cracked to varying degrees upon removal from the experimental setup thereby preventing post-FS examinations on intact pellets.

2.3. Post flash sintering characterization

The resulting high-density pellets were characterized by geometric density measurements followed by cutting and polishing the specimens along their longitudinal cross-section (approximately one half of the diameter was removed in an effort to minimize possible surface artifacts) to evaluate their microstructure. The volume assumed for geometric density determination of the FS materials was calculated based on the summation of two conical frustum geometries that represented the hourglass shape of the final geometry. XRD measurements were performed on the polished samples to determine the final phase of the resulting material after FS. The XRD measurements were performed using a Bruker AXS D8 Advance X-ray diffractometer, Cu-K radiation, and θ-2θ geometry. The X-ray diffractometer was equipped with a Göebel mirror to achieve parallel beam diffraction optics. The 2θ scans were performed using fixed incidence angle of 10° using a step size of 0.02° and a dwell time of 3 s per step, over a 2θ range of 20°—80°. Calibration of the instrument θ position was performed using a NIST 1976 Corundum standard following a company-established protocol. The company specification ($\pm$ 0.02°) for the configuration of the diffractometer used in this investigation was achieved. Using this calibration protocol, the error in lattice parameter measurements is $\pm$ 0.001 Å. Peak indexing was done in the same manner as discussed in section 2.1. Lastly, to observe the materials
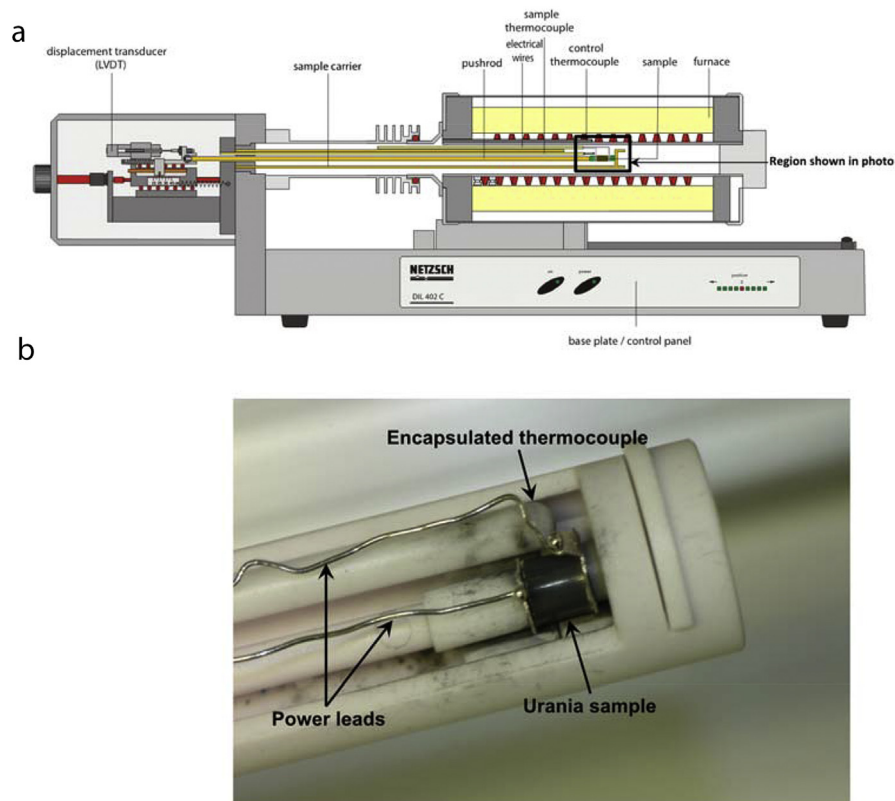

Fig. 2. (a) Schematic diagram showing the main components of the flash sintering experimental setup which was used in this study, (b) A photo of the actual measurement assembly showing the encapsulated thermocouple and platinum wires and leads in contact with a UO$_{2.16}$ pellet.

microstructure produced by FS, an Inspect F scanning electron microscope (SEM) operating in secondary electron mode was used to acquire images across the entire length of polished FS samples.

3. Results and discussion

The results from FS measurements, post-FS XRD and microstructural characterization on the $UO_{2.16}$ and $UO_{2.00}$ pellets will be discussed sequentially in the following sections, along with a comparison between densification obtained from FS and conventional sintering.

3.1. Pellet fabrication via flash sintering

Fig. 3 shows the density (black line) and furnace temperature (blue dotted line) evolution during FS on a $UO_{2.16}$ (a) and a $UO_{2.00}$ (b) pellet. In the case of the $UO_{2.16}$ pellet (Fig. 3(a)), a field of 188 V/cm and a current density of 632 mA/mm^2 were applied for 123 s. The $UO_{2.00}$ pellet (Fig. 3(b)) was flash sintered under the same field (188 V/cm) but at a lower current density, 442 mA/mm^2, for 185 s. The furnace temperature for both FS tests was kept constant at 600 °C before flash sintering. Region I in Fig. 3(a) and (b) indicates the time before the application of the field during which the samples are left to equilibrate at the specified furnace temperature. Region II indicates when FS takes place, that is the application of the 188 V/cm field and the subsequent change into current controlled mode. The start of FS corresponds to an instantaneous densification onset followed by a more gradual increase in density to a peak value of 91% TD for the $UO_{2.16}$ pellet and 81% TD for the $UO_{2.00}$ pellet. An increase in temperature, as measured by an alumina-sheathed thermocouple in close proximity to the pellets (Fig. 2(b)), is also observed in region II, for both pellets. In Fig. 3(a) the temperature rises to a peak value of 835 °C while in Fig. 3(b) the maximum temperature reached during FS is 780 °C. Lastly, region III indicates when the power is instantaneously removed from the sample by turning off the power supply. Following region III, a small decrease in density is evident as the temperature begins to drop until it returns to the 600 °C equilibrium temperature it was at before FS.

As evident from Fig. 3, an increase in furnace temperature was observed during FS for both pellets. This is due to Joule heating in the sample from the application of current and is commonly observed in the literature [11,28,41]. The increase in temperature is fairly similar between the two pellets, 55 °C difference, despite a large discrepancy in the applied current densities; 632 mA/mm^2 for

the $UO_{2.16}$ pellet versus 442 mA/mm^2 for the $UO_{2.00}$ pellet. This is an interesting observation as it indicates that the sample resistivity can largely affect the observed heating. One would expect that a 1.5 times higher current density would result in a similar increase in temperature but this is not the case here as the $UO_{2.16}$ pellet (FS at a current density 1.5 times higher than the $UO_{2.00}$ pellet) only shows a 1.07 times increase in temperature. This discrepancy can be explained by taking into account the resistivity of $UO_{2.00}$ which is much higher than that of UO_{2+x} [28,42,43]. This means that when FS under the same current density, a $UO_{2.00}$ sample would heat up more than the UO_{2+x} sample.

Nonetheless, the temperatures shown in Fig. 3 are only to be taken as an estimate since the encapsulated thermocouple is next to, ~2 mm away, and not in contact with the sample. Therefore, the sample temperatures reached during FS are estimated to be higher than those measured using the current setup. A more accurate specimen temperature could have been measured with a pyrometer, as was done in other studies by Raj [11] and Francis et al. [44], but due to the constraints of the measurement apparatus this was not possible. In both aforementioned studies, there was agreement that application of an electric field does increase the temperature but not to such temperatures required to sinter the materials in such a short time as observed during FS. These studies concluded that although Joule heating plays a role during FS, there may be other mechanisms that are also synergistically taking place to achieve the ultrafast sintering observed during FS. In another investigation focused on in-situ flash sintering experiments performed on 3 Yttria stabilized zirconia (YSZ), LeBrun et al. [7] used XRD on a platinum thin-film, placed on the surface of the samples, to measure the lattice expansion (and relate that to temperature) due to FS induced heating. These measurements on the expansion of the Pt lattice parameter showed that the material increased from the starting 1000 °C temperature by ~300 °C during FS at a current density of 105 mA/mm^2. These measured values are considered to be fairly accurate due to the well-established thermal expansion data on platinum. In this study the applied current densities (442 for the $UO_{2.00}$ pellet and 632 mA/mm^2 for the $UO_{2.16}$ pellet) were higher than in the above cited works, therefore, it is possible the actual sample temperatures are underestimated more severely.

To further evaluate the heating of the materials during FS, the sample temperature was estimated using the method to calculate the joule heating based on power density described by Raj [11]. For this methodology, we used the power density achieved during the steady state dwell segment (region II) in Fig. 3(a) and (b). During
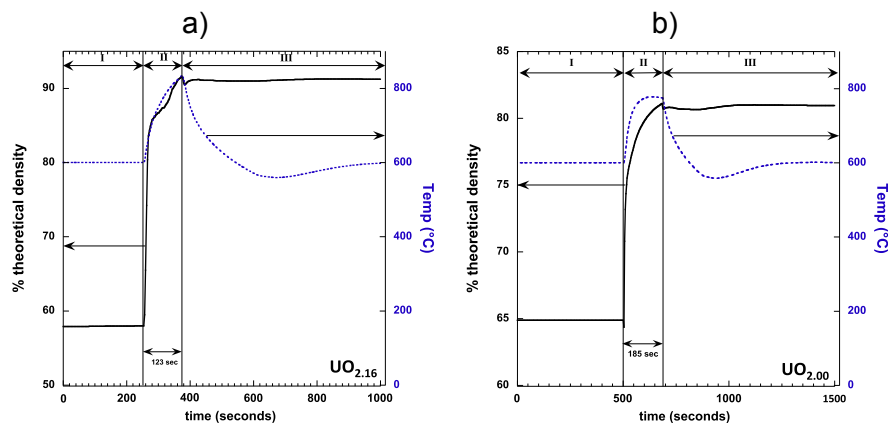

Fig. 3. Density (black solid line) and furnace temperature (blue dotted line) evolution of a $UO_{2.16}$ pellet flash sintered under a field of ~188 V/cm and a current density of 632 mA/mm^2 (a) and a $UO_{2.00}$ pellet flash sintered under a field of ~188 V/cm and a current density of 442 mA/mm^2 (b). Both pellets were flash sintered at an iso-thermal furnace temperature of 600 °C. (For interpretation of the references to colour in this figure legend, the reader is referred to the Web version of this article.)

this region after the flash event when the power density achieves a steady state, the sample can be considered to be in a joule heating regime. During the steady state segment of the experiment the calculated power for UO_{2+x} was $P_{dwell} = 200$ W and for $UO_{2.00}$ was $P_{dwell} = 105$ W. The estimated black body radiation temperatures calculated during the steady dwell was 2061 °C for UO_{2+x} and 1733 °C for $UO_{2.00}$. The calculated temperature values are likely overestimated, due to several points. First, the electrodes and wire supplying the power during flash sintering are made of platinum with a listed meting point (T_m) of 1768 °C, therefore if the specimens were exposed to a temperature of the magnitudes calculated it would be expected to observe signs of melting of the Pt electrode. Inspection of the Pt to sample interface showed no signs of melting in either material. Based on this is can be assumed that the temperature of the sample conservatively lies between the range of 800 °C (measured from the TC next to the sample) and less than 1768 °C. The primary reason for this discrepancy is, in using this concept to estimate temperature the assumption is made that our experimental geometry is an ideal black body radiator, which it is not. In the current experimental setup the sample is pinned between platinum contact points connected to wires in contact with alumina platens offering ample paths to dissipate conductive heat. Therefore it is likely some of the applied power is conducting away from the specimen at a faster rate than that which is absorbed. In contrast to the experimental geometry used in this investigation, the experimental geometry used during Raj [11], the sample is hanging in free space by two small wires thereby making the ideal situation for more accurate black body radiation temperature calculations in that there are no other primary thermal conduction mechanisms taking place.

The FS results from the $UO_{2.16}$ and $UO_{2.00}$ pellets showed that, for both materials, moderate temperature combined with application of an electric field produces exceptionally high sintering rates that result in a high degree of densification at furnace temperatures where little to no sintering occurs using conventional methods. As mentioned earlier, the two different power densities (produced by keeping applied field strength constant while varying current density) used to FS the two pellets, were determined to produce maximum density in fully intact pellets. Using higher power density values than the ones presented here, caused the specimens to crack. For example, when FS was performed on a $UO_{2.16}$ pellet using a field of 188 V/cm and a current density of 694 mA/mm^2, a density of 93% TD was achieved but the pellet cracked during measurements. Similarly, $UO_{2.00}$ pellets that were FS under current densities greater than 442 mA/mm^2, fractured catastrophically into multiple pieces.

3.2. Post flash sintering characterization

3.2.1. X-ray diffraction

XRD was performed to assess the effect of FS on the materials crystallographic assemblage. Fig. 4 shows the XRD patterns obtained from the $UO_{2.16}$ and $UO_{2.00}$ pellets before FS (black line) and after FS (red line). In both cases, the XRD patterns corresponding to the materials in the pre-FS condition were obtained from the as-received (Fig. 4(a)) and fully reduced (Fig. 4(b)) AREVA feedstocks.

XRD measurements revealed that the pre-FS starting material for the $UO_{2.16}$ pellet (Fig. 4(a)) was mixed phasic, comprised of both of a major fluorite (red markers) phase with a measured lattice parameter of 5.46394 ± 0.001 Å and a lower percentage of α-U_3O_8 (blue markers). The above mentioned phases were identified by indexing them with respect to the following JCPDF cards face centered cubic $UO_{2.13}$ #074–2432 (red markers) and body centered orthorhombic U_3O_8 #031–1424 (blue markers). Additional "F" markers corresponding to the fluorite phase peak positions are shown as an aide in distinguishing between the two separate phases. The XRD pattern obtained from the polished post-FS $UO_{2.16}$ pellet (Fig. 4(a)) shows that the minor U_3O_8 phase, which was initially present in the pre-sintered material, was consumed during FS. Indexing of the post-FS pellet shows that the flash process produced a monophasic cubic fluorite material with a lattice parameter of 5.4584 ± 0.001 Å as indexed with respect to JCPDF card #078–0725 (red markers) for $UO_{2.00}$ with a listed lattice parameter of 5.4660 Å. This result shows that the two-phase urania is converted to a single-phase fluorite structure consistent with a sample temperature above ~800 °C [31]. The two-phase, $UO_{2.16}+U_3O_8$, structure does not appear after cooldown presumably because the sample underwent an overall change in stoichiometry during FS or because the cooling rate was sufficiently high to prevent re-formation of the initial two-phase structure for UO_{2+x}. Regarding the change in lattice parameter observed in the pre-FS and post-FS material, we believe the change in stoichiometry is a contributor, but we must not rule out other factors that may also contribute to this, such as defect elimination, internal stresses and strain gradients.

The pre-FS XRD patterns corresponding to the fully reduced feedstock (Fig. 4(b)) show a monophasic cubic fluorite that indexes favorably with JPCF card #078–0725 for $UO_{2.00}$ (red markers). As in the case of the previously discussed as received material, "F" markers corresponding to the fluorite phase peak positions are shown on the plot. Also shown in Fig. 4(b) is the XRD pattern obtained from the $UO_{2.00}$ pellet, post-FS, showing very little change from the pre-FS material. The post-FS material is a cubic fluorite

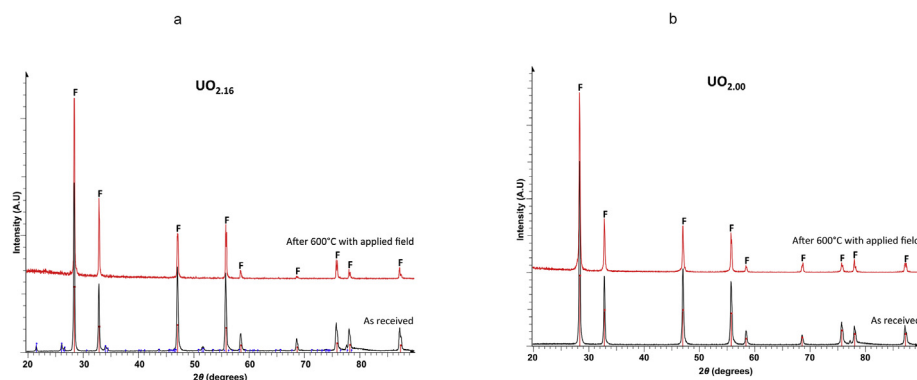**Fig. 4.** XRD patterns obtained in the pre (black line) and post (red line) FS condition for a $UO_{2.16}$ (a) and a $UO_{2.00}$ (b) pellet. Additional "F" markers corresponding to the fluorite phase peak positions are shown as an aide in distinguishing between the two separate initial phases (a) and showing the principal fluorite phase (b). (For interpretation of the references to colour in this figure legend, the reader is referred to the Web version of this article.)

phase that is very similar to the pre-FS material except for a small change in lattice parameter from 5.46408 ± 0.001 Å to 5.46702 ± 0.001 Å in the post-FS material. This small change in lattice may be due to a slight reduction in O/M or strain produced during FS. While both starting feedstocks had a sub-micron grain size, in both sets of XRD patterns of Fig. 4(a) and (b), almost no change in grain size was evident when comparing diffraction maxima peak widths. Because the XRD measurement sampled the entire cross section of the pellet, SEM examination was used to further characterize the microstructure. Finally, upon comparing the post-FS XRD patterns for the $UO_{2.16}$ and $UO_{2.00}$ pellets, both materials are very similar with regards to both phase and chemistry.

3.2.2. Microstructure

In Fig. 5 the SEM micrographs of polished cross-sections from the $UO_{2.16}$ (a) and $UO_{2.00}$ (b) pellets are shown. The images reveal non-uniform microstructures for both pellets with density gradients along the longitudinal axis of each pellet. For the $UO_{2.16}$ sample (Fig. 5(a)), the image shows regions of lower density on the two ends of the pellet, where the electric field was applied, and a region of high density in the central area of the pellet. A magnified view of the high-density central region, outlined with a box from the $UO_{2.16}$ pellet is also shown in Fig. 5(a). The higher magnification image shows a distribution of grains ranging in size from 1 to 15 μm with some intragranular and intergranular porosity.

The final microstructure of the $UO_{2.00}$ pellet (Fig. 5(b)) is highly fractured along its length. The nature of the cracking is indicative of defects that are not unexpected when pressing this O/M-adjusted feedstock without binder or lubricant (also seen to a lesser extent for the $UO_{2.16}$ pellet in Fig. 5(a)). The outer edges of the $UO_{2.00}$ pellet show a more uniform microstructure, containing fewer defects than the central part of the pellet, and cracks that can be associated with differential shrinkage can also be seen. A magnified view of this outer region of the $UO_{2.00}$ pellet is also shown in Fig. 5(b). This magnified view shows intragranular porosity, pores along the grain boundaries and grain sizes ranging from 1 to 15 μm, similarly to the $UO_{2.16}$ pellet (Fig. 5(a)). In contrast to the $UO_{2.16}$ pellet, a higher volume fraction of porosity networks was present. Finally, the post-FS geometry for both pellets changed into an hourglass shape, although this was more profound in the $UO_{2.00}$ pellet (Fig. 5(b)).

It can be presumed that the irregular shape and cracks observed in both FS specimens are most likely due to the following factors. These factors include the mechanical constraint coupled with the heat sink effect in the experimental setup may lead to differential shrinking rates (within the sample) and thermal gradients from contact with the electrodes. Another factor is, as a result of using binderless and lubricant free cold uniaxial pressing to prepare specimens for FS, it is likely that post pressing defects (microcracks)
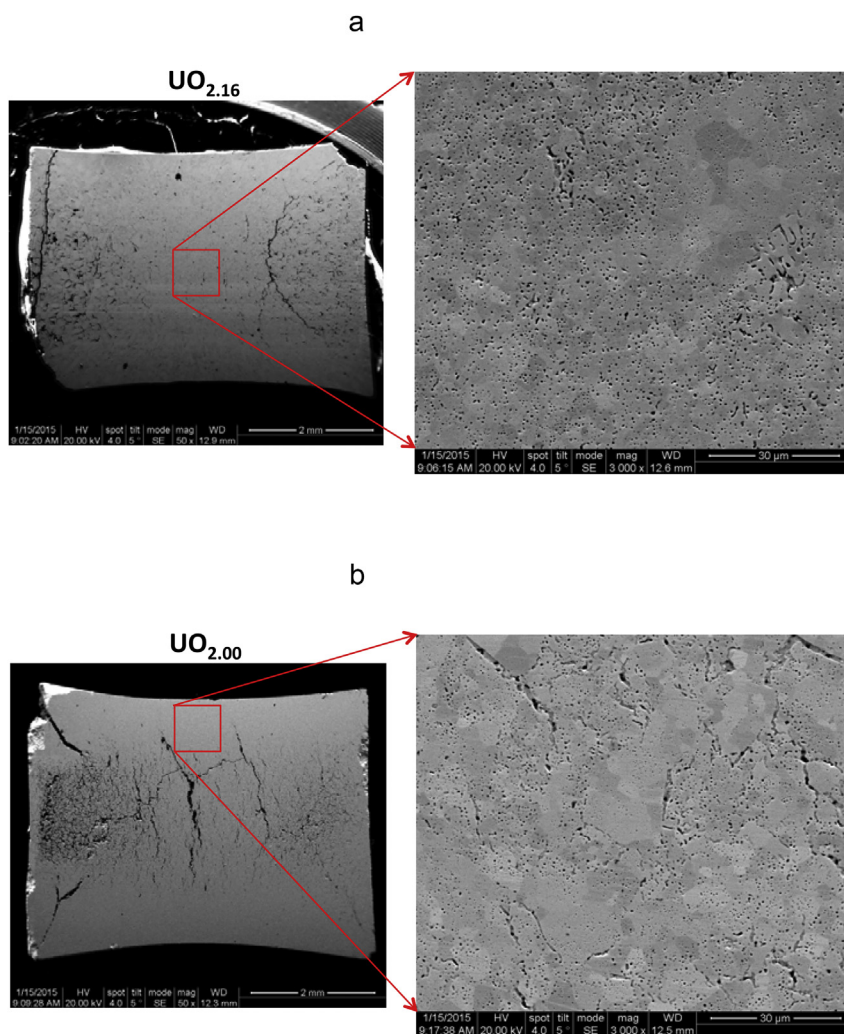

Fig. 5. Low magnification SEM images obtained across the longitudinal cross-section of a $UO_{2.16}$ (a) and $UO_{2.00}$ (b) pellet. For each respective low magnification image, the boxes show the highest density region from which the high magnification images (indicated with arrows) were obtained.

and density variation consisting of higher density at the ends of the pellets and lower density towards the center exists within the pre-FS materials. As a consequence of the preexisting defects and density variation in the pressed pellets it is reasonable to assume the FS materials would exhibit some signature of these pressing artifacts.

The microstructural examination shows that during FS, densities and grain sizes relevant to LWR fuels can be rapidly achieved even at low furnace temperatures, however, as indicated by the heterogeneous microstructures and the abundance of retained intragranular porosity, substantial improvement in process control is necessary to be able to achieve coupled density and microstructure control.

3.3. Flash sintering versus conventional sintering

Comparisons between pellets flash sintered at 600 °C and pellets sintered at various temperatures using conventional, pressureless, sintering were carried out for $UO_{2.00}$ and $UO_{2.16}$ to elucidate the differences. Three temperature conditions were selected for conventional sintering tests; 600, 1000 and 1650 °C. Note that although the instrument was programed to achieve a final temperature 1650 °C the plots shown in Fig. 6 are meant to show the point in the 10 °C/min ramp when the equivalent sintering strain to the FS material was achieved. In these tests, the temperature was ramped up at a rate of 10 °C/min until the desired temperature was reached, after which it was held in an isothermal step for up of 2 h and cooled at 10 °C/min. None of the plots in Fig. 6 show the ramp down to ambient temperature. The conventional and flash sintering data were plotted as a function of sintering strain, ((length$_{final}$-length$_{initial}$)/length$_{final}$ (%)) versus time to show the pure linear shrinkage measured in-situ during the series of dilatometer sintering measurements. In Fig. 6(a) the evolution of the shrinkage strain in $UO_{2.16}$ pellets due to FS at 600 °C (black line) and conventional sintering at 600 °C (blue squares), 1000 °C (red triangles) and 1650 °C (green diamonds) is shown. In Fig. 6(b) the

same data is shown for $UO_{2.00}$ pellets. All plots in Fig. 6 were adjusted so that time equal to zero corresponds to when samples were heated to 600 °C. The amount of time required to meet the conditions discussed in the following text are based from the measurements beginning at 600 °C unless otherwise indicated.

The plots in Fig. 6(a) show that rapid shrinkage (densification) takes place during the 123 s of FS at 600 °C, whereas in the sample sintered conventionally under the same temperature almost no change was observed, even after holding the sample at temperature for over 4650 s. This same behavior was observed for the $UO_{2.00}$ pellets that were conventionally and flash sintered at 600 °C (see Fig. 6(b)). As also seen from the calculated density results presented in section 3.1, the final sintering strain measured for the flash sintered $UO_{2.00}$ pellet was less than that recorded for the flash sintered $UO_{2.16}$ pellet. Expectedly, based upon the established differences in the sinterability of UO_{2+x} versus $UO_{2.00}$ [45–47], the total time to reach maximum shrinkage during FS for UO_{2+x} was less than for $UO_{2.00}$; 123 versus 185 s.

As expected, for temperatures above 600 °C it was observed that during the heating stage of conventional sintering, the material starts to sinter. For example, increasing the temperature from 600 to 1000 °C, results in an approximate 10% increase in shrinkage strain, for a $UO_{2.16}$ pellet (see Fig. 6(a)). When the target sintering temperature is reached, 1000 °C in this case (red circle), the pellet continues to sinter until finally reaching a sintering strain equivalent to that achieved via FS at 600 °C. The equivalent sintering strain value is indicated with an "x" as projected by the dotted line from the termination of the FS at 600 °C measurement. Nonetheless, for a $UO_{2.16}$ pellet to reach a shrinkage strain equivalent to that of FS conventionally, 1.7 h were required as compared to 123 s. This is despite conventional sintering performed at a temperature 400 °C higher than for FS. Similarly, significant shrinkage was observed when ramping up from 600 to 1650 °C. In this case, the temperature and time required to reach the maximum sintering strain as achieved via FS was 1044 °C (green circle) over a period of 2950 s. Conventional sintering continues past this temperature shown on
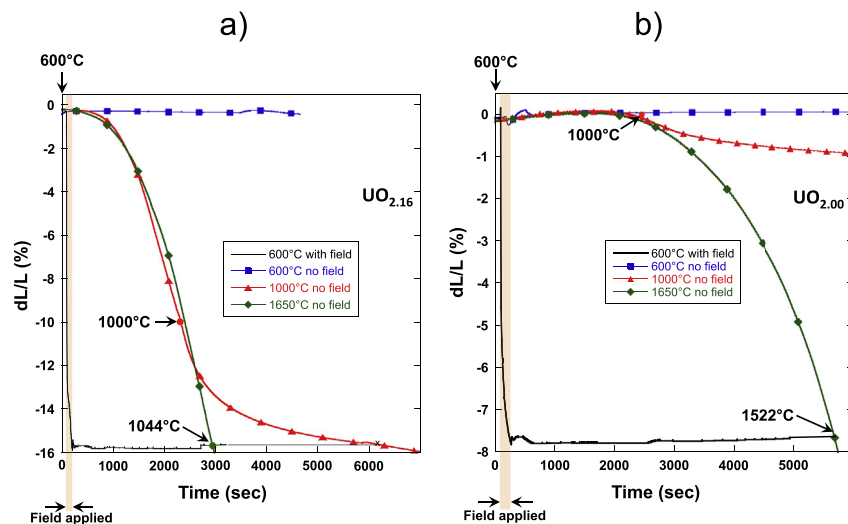

Fig. 6. Sintering strain evolution (ramp rate of 10 °C/min) achieved via FS at 600 °C and conventional sintering at programmed isothermal temperatures to 600 °C (blue squares), 1000 °C (red triangles) and 1650 °C (green diamonds) for $UO_{2.16}$ (a) and $UO_{2.00}$ (b) pellets. For both FS materials at the 600 °C a high degree of sintering strain took place during field application while no apparent sintering was observed in materials during the 600 °C isotherm without applied field. Regarding the 1000 °C isotherm condition (onset labeled with a dot and arrow) for $UO_{2.16}$, sintering strain equivalent to the value seen in FS-$UO_{2.16}$ was attained in 64 min at the isotherm. The equivalent sintering strain value is indicated with an "x" as projected by a dotted line from the termination of the FS at 600 °C measurement. For $UO_{2.00}$ exposed to the 1000 °C isotherm (onset labeled with a dot and arrow), the equivalent sintering strain to FS-$UO_{2.00}$ was not attained. In contrast to the 1000 °C measurements, the profiles for the programmed 1650 °C isotherm condition do not show when the isotherm is reached in either 6a or 6b. Instead, the profiles are labeled showing the temperature (during the ramp) at which the equivalent final strain to 600 °C FS material was achieved. The ramp down to ambient temperature is not shown in Fig. 6. (For interpretation of the references to colour in this figure legend, the reader is referred to the Web version of this article.)

the plots but since the aim here was to compare the conditions that produce a shrinkage equivalent to that achieved during FS, the plot was stopped shortly past that point thereby not showing when the 1650 °C isothermal step was reached.

The identical measurements that were previously discussed were also performed on $UO_{2.00}$ pellets (see Fig. 6(b)). The $UO_{2.00}$ pellets tested here exhibit significantly less shrinkage, under conventional sintering and FS conditions, when compared to $UO_{2.16}$ pellets. More specifically, the final sintering strain reached during FS of a $UO_{2.00}$ pellet at 600 °C (furnace temperature) was not achieved over the time scale of our measurements for conventional sintering at 1000 °C (red circle). To achieve a sintering strain equal to the maximum achieved for FS, conventional heating to 1522 °C (green circle) over a period of approximately 1.6 h was required.

The results discussed here illustrate that there are indeed interesting phenomena associated with FS as compared to conventional sintering. Fig. 6(a) and (b) demonstrate that materials exposed to electric field combined with modest furnace temperatures can sinter in much shorter times and at substantially lower temperatures as compared to conventional sintering. The results also show that, as commonly observed in conventional sintering [45–47], hyper-stoichiometry also increases sintering kinetics during the ultrafast sintering seen under applied electric fields. During FS, UO_{2+x} samples can tolerate exposure to higher current densities than $UO_{2.00}$ samples while producing fully intact pellets correspondingly with higher densities. Various mechanisms have been proposed in the literature for the very high sintering rates observed in FS at nominally low processing temperatures, such as joule heating, point defect multiplication and metastable phase formation [1,40,48]. Observations from the studies reported here, however, were not able to establish which mechanisms are responsible for the flash sintering behavior seen in urania. Additional studies will be required to establish the mechanisms underlying the greatly enhanced sintering kinetics as well as to establish the process control necessary to employ the flash sintering technique to sinter urania with controlled densities and microstructures.

4. Conclusions

Flash sintering was performed on pellets of hyper-stoichiometric and stoichiometric urania. Two different conditions were identified that produced an intact pellet with the highest density for each material at a furnace temperature of 600 °C. In a $UO_{2.16}$ pellet, using 188 V/cm and 632 mA/mm^2 for 123 s produced a final sintered density of 91% TD and for a $UO_{2.00}$ pellet using 188 V/cm and 442 mA/mm^2 for 185 s produced a final sintered density of 81% TD. Using current densities in excess of these values was shown to cause catastrophic failure for each material.

XRD revealed that after FS, the initial mixed phase $UO_{2.16}$ material was converted into a monophasic cubic fluorite material. XRD measurements on the $UO_{2.00}$ material showed that it remained relatively unchanged from its starting phase, remaining a cubic fluorite phase similar to the FS hyper-stoichiometric material.

SEM characterization on polished longitudinal cross-sections of FS $UO_{2.16}$ and $UO_{2.00}$ pellets showed microstructures consisting of regions of porosity and regions of high-density material. The porous and high-density areas were localized at different regions within each pellet depending on its stoichiometry. In the hyper-stoichiometric material, the defects were mainly concentrated on the two ends of the pellet, where the electric field was applied, and a uniform, high-density region was observed across the central core of the pellet. In the stoichiometric pellet, the defects were shown to be concentrated across the central core and on both ends of the pellet. A region of high-density material was observed in the outer circumference of the pellet.

Lastly, dilatometer measurements comparing FS to conventional sintering showed that different sintering characteristics occur based on the stoichiometry of each pellet. In hyper-stoichiometric samples, an equivalent sintering strain achieved during FS for approximately 2 min can be achieved when sintering conventionally by heating to 1000 °C and holding slighty over 60 min or heating to 1044 °C. In stoichiometric urania an equivalent sintering strain to FS was not achieved when sintering at 1000 °C. A similar sintering strain to that achieved during FS for about 3 min was only possible by heating to 1522 °C.

The data in this investigation show that in flash sintered materials densification occurs in a short period while the equivalent sintering without an applied field requires longer times and/or significantly higher temperatures; 91% TD with ~10 μm grain size was achieved in minutes at a temperature of 0.3 of the (T_m) as opposed to several hours at $0.6T_m$ for a conventionally sintered fuel pellet. In this work, we have fabricated high density UO_2 pellets with the presence of an electric field at temperatures much lower than typically used to sinter UO_2, although with non-uniform microstructures. Further work needs to be done to identify the experimental parameters and mechanisms responsible for enhanced sintering kinetics, which in turn can enable control of microstructure uniformity and grain growth in flash sintered pellets.

Appendix A. Supplementary data

Supplementary data related to this article can be found at https://doi.org/10.1016/j.jnucmat.2018.03.049.

References

[1] R. Raj, M. Cologna, J.S.C. Francis, Influence of externally imposed and internally generated electrical fields on grain growth, diffusional creep, sintering and related phenomena in ceramics, J. Am. Ceram. Soc. 94 (7) (2011) 1941–1965.

[2] L. Ge, G. Subhash, R.H. Baney, J.S. Tulenko, E. McKenna, Densification of uranium dioxide fuel pellets prepared by spark plasma sintering (SPS), J. Nucl. Mater. 435 (1–3) (2013) 1–9.

[3] H. Muta, K. Kurosaki, M. Uno, S. Yamanaka, Thermal and mechanical properties of uranium nitride prepared by SPS technique, J. Mater. Sci. 43 (19) (2008) 6429–6434.

[4] A.J. Mackie, G.D. Hatton, H.G.C. Hamilton, J.S. Dean, R. Goodall, Carbon uptake and distribution in Spark Plasma Sintering (SPS) processed Sm (Co, Fe, Cu, Zr) z, Mater. Lett. 171 (2016) 14–17.

[5] T. Yao, S.M. Scott, G. Xin, J. Lian, TiO2 doped UO2 fuels sintered by spark plasma sintering, J. Nucl. Mater. 469 (2016) 251–261.

[6] H. Muta, K. Kurosaki, M. Uno, S. Yamanaka, Thermophysical properties of several nitrides prepared by spark plasma sintering, J. Nucl. Mater. 389 (1) (2009) 186–190.

[7] J. Lebrun, T.G. Morrissey, J.S.C. Francis, K.C. Seymour, W.M. Kriven, R. Raj, Emergence and Extinction of a New Phase during On-off Experiments Related to Flash Sintering of 3YSZ, vol. 1497, 2015.

[8] J.S.C. Francis, M. Cologna, R. Raj, Particle size effects in flash sintering, J. Eur. Ceram. Soc. 32 (12) (2012) 3129–3136.

[9] M. Cologna, B. Rashkova, R. Raj, Flash sintering of nanograin zirconia in <5 s at 850 °C, J. Am. Ceram. Soc. 93 (11) (2010) 3556–3559.

[10] R. Raj, Analysis of the power density at the onset of flash sintering, J. Am. Ceram. Soc. 3232 (2016) 3226–3232.

[11] R. Raj, Joule heating during flash-sintering, J. Eur. Ceram. Soc. 32 (10) (2012)

2293—2301.

[12] E. Zapata-Solvas, S. Bonilla, P.R. Wilshaw, R.I. Todd, Preliminary investigation of flash sintering of SiC, J. Eur. Ceram. Soc. 33 (13—14) (2013) 2811—2816.

[13] S. Grasso, et al., Modeling of the temperature distribution of flash sintered zirconia, J. Ceram. Soc. Jpn. 119 (1386) (2011) 144—146.

[14] H. Yoshida, K. Morita, B.N. Kim, Y. Sakka, T. Yamamoto, Reduction in sintering temperature for flash-sintering of yttria by nickel cation-doping, Acta Mater. 106 (2016) 344—352.

[15] A. Karakuscu, et al., Defect structure of flash-sintered strontium titanate, J. Am. Ceram. Soc. 95 (8) (2012) 2531—2536.

[16] E. Bichaud, J.M. Chaix, C. Carry, M. Kleitz, M.C. Steil, Flash sintering incubation in Al2O3/TZP composites, J. Eur. Ceram. Soc. 35 (9) (2015) 2587—2592.

[17] A. Gaur, V.M. Sglavo, Flash-sintering of MnCo2O4 and its relation to phase stability, J. Eur. Ceram. Soc. 34 (10) (2014) 2391—2400.

[18] J.G. Pereira Da Silva, J.M. Lebrun, H.A. Al-Qureshi, R. Janssen, R. Raj, Temperature distributions during flash sintering of 8% yttria-stabilized zirconia, J. Am. Ceram. Soc. 98 (11) (2015) 3525—3528.

[19] J.A. Downs, V.M. Sglavo, Electric field assisted sintering of cubic zirconia at 390 °C, J. Am. Ceram. Soc. 96 (5) (2013) 1342—1344.

[20] I.J. Hewitt, A.A. Lacey, R.I. Todd, A mathematical model for flash sintering, Math. Model Nat. Phenom. (2015) 1—16.

[21] D. Byler, Report on Field Assisted Sintering of High Uranium Density Ceramic Fuels, Assessing Voltage and Current Effects, 2015.

[22] X. Yang, J. Gao, Y. Wang, X. Chang, Low-temperature sintering process for UO2 pellets in partially-oxidative atmosphere, Trans. Nonferrous Metals Soc. China (Engl. Ed.) 18 (1) (2008) 171—177.

[23] N. Fuhrman, L.D. Hower, R.B. Holden, Low-temperature sintering of uranium dioxide, J. Am. Ceram. Soc. 46 (3) (1963).

[24] J. Gao, X. Yang, R. Li, Y. Wang, F. Zhong, Low-temperature sintering mechanism on uranium dioxide, J. Mater. Sci. 42 (15) (2007) 5936—5940.

[25] S.K. Jha, R. Raj, The effect of electric field on sintering and electrical conductivity of titania, J. Am. Ceram. Soc. 97 (2) (2014) 527—534.

[26] H. Yoshida, Y. Sakka, T. Yamamoto, J.M. Lebrun, R. Raj, Densification behaviour and microstructural development in undoped yttria prepared by flash-sintering, J. Eur. Ceram. Soc. 34 (4) (2014) 991—1000.

[27] M. Cologna, J.S.C. Francis, R. Raj, Field assisted and flash sintering of alumina and its relationship to conductivity and MgO-doping, J. Eur. Ceram. Soc. 31 (15) (2011) 2827—2837.

[28] A.M. Raftery, J.G.P. da Silva, D.D. Byler, D.A. Andersson, B.P. Uberuaga, C.R. Stanek, Onset conditions for flash sintering of UO2, J. Nucl. Mater. 493 (2017) 264—270.

[29] R. Raj, Analysis of the power density at the onset of flash sintering, J. Am. Ceram. Soc. 7 (2016) 1—7.

[30] H. Idriss, Surface reactions of uranium oxide powder, thin films and single crystals, Surf. Sci. Rep. 65 (3) (2010) 67—109.

[31] J.D. Higgs, W.T. Thompson, B.J. Lewis, S.C. Vogel, Kinetics of precipitation of U4O9 from hyperstoichiometric UO2+x, J. Nucl. Mater. 366 (3) (2007) 297—305.

[32] R.H. French, S.J. GLass, F.S. Ohuchi, Y.-N. Xu, W.Y. Ching, Experimental and theoretical determination of the electronic structure and optical properties of three phases of ZrO2, Phys. Rev. B 49 (8) (1994) 5133—5142.

[33] J.C. Garcia, et al., Structural, electronic, and optical properties of ZrO2 from ab initio calculations, J. Appl. Phys. (2006) 1—25.

[34] ASTM, ASTM C1430—07 (2011), Standard Test Method for Determination of Uranium, Oxygen to Uranium (O/U), and Oxygen to Metal (O/M) in Sintered Uranium Dioxide and Gadolinia-uranium Dioxide Pellets by Atmospheric Equilibration, 2011.

[35] Bruker, Bruker Evaluation (EVA) Program, 2005.

[36] JCPDS, International Centre for Diffraction Data, 1974.

[37] M. Cologna, A.L.G. Prette, R. Raj, Flash-sintering of cubic yttria-stabilized zirconia at 750 °C for possible use in SOFC manufacturing, J. Am. Ceram. Soc. 94 (2) (2011) 316—319.

[38] A.L.G. Prette, M. Cologna, V. Sglavo, R. Raj, Flash-sintering of Co2MnO4 spinel for solid oxide fuel cell applications, J. Power Sources 196 (4) (2011) 2061—2065.

[39] X. Hao, Y. Liu, Z. Wang, J. Qiao, K. Sun, A novel sintering method to obtain fully dense gadolinia doped ceria by applying a direct current, J. Power Sources 210 (2012) 86—91.

[40] J.S.C. Francis, R. Raj, Influence of the field and the current limit on flash sintering at isothermal furnace temperatures, J. Am. Ceram. Soc. 96 (9) (2013) 2754—2758.

[41] R.I. Todd, E. Zapata-Solvas, R.S. Bonilla, T. Sneddon, P.R. Wilshaw, Electrical characteristics of flash sintering: thermal runaway of Joule heating, J. Eur. Ceram. Soc. 35 (2015) 1865—1877.

[42] P. Garcia, et al., A defect model for UO2+x based on electrical conductivity and deviation from stoichiometry measurements, J. Nucl. Mater. 494 (2017) 461—472.

[43] P. Ruello, G. Petot-Ervas, C. Petot, L. Desgranges, Electrical conductivity and thermoelectric power of uranium dioxide, J. Am. Ceram. Soc. 88 (3) (2005) 604—611.

[44] J.S.C. Francis, R. Raj, Flash-Sinterforging of nanograin zirconia : field assisted sintering and superplasticity, J. Am. Ceram. Soc. 95 (1) (2012) 138—146.

[45] H. Assmann, W. Dörr, M. Peehs, Control of UO2 microstructure by oxidative sintering, J. Nucl. Mater. 140 (1986) 0—5.

[46] T.R.G. Kutty, et al., Densification behaviour of UO2 in six different atmospheres, J. Nucl. Mater. 305 (2—3) (2002) 159—168.

[47] H. Matzke, Atomic transport properties in UO2 and mixed oxides (U, Pu)O2, J. Chem. Soc. 83 (1987) 1121—1142.

[48] R. Baraki, S. Schwarz, O. Guillon, Effect of electrical field/current on sintering of fully stabilized zirconia, J. Am. Ceram. Soc. 95 (1) (2012) 75—78.